

Article

Computational Design Optimization for S-Ducts

Alessio D'Ambros ¹, Timoleon Kipouros ^{*,1} , Pavlos Zachos ¹, Mark Savill¹ and Ernesto Benini ²¹ School of Aerospace, Transport and Manufacturing, Cranfield University, Cranfield, MK43 0AL, UK² Department of Industrial Engineering, University of Padova, 35131 Padova, Italy

* Correspondence: t.kipouros@cranfield.ac.uk; Tel.: +44-1234-758237

Version September 13, 2018 submitted to MDPI

Abstract: In this work, we investigate the computational design of a typical S-duct that is found in the literature. We model the design problem as a shape optimization study. The design parameters describe the 3D geometrical changes to the shape of the S-duct and we assess the improvements to the aerodynamic behavior by considering two objective functions: the pressure losses and the swirl. The geometry management is controlled with the Free-Form Deformation (FFD) technique, the analysis of the flow is performed using steady-state computational fluid dynamics (CFD), and the exploration of the design space is achieved using the heuristic optimization algorithm Tabu Search (MOTS). The results reveal potential improvements by 14% with respect to the pressure losses and by 71% with respect to the swirl of the flow. These findings exceed by a large margin the optimality level that was achieved by other approaches in the literature. Further investigation of a range of optimum geometries is performed and reported with a detailed discussion.

Keywords: S-duct design; computational design; stochastic optimization; Tabu Search; Free Form Deformation

1. Introduction

S-shaped ducts of rectangular or circular cross-section have been widely investigated to better understand and characterize the flow field inside them at different inlet condition. In particular, for their potential contribution in noise and drag reduction, S-Ducts as aero-engine intakes are of great interest in the propulsion field.

Liebeck [1] widely illustrated how a blended wing body configuration can be a potential breakthrough in subsonic transport efficiency. However, propulsion systems highly integrated with the air-frame, employing an S-Duct as intake diffuser, are affected by high levels of flow unsteadiness and distortion. This is driven by secondary flow and local flow separation due to the adverse pressure gradient typical of curved intakes. The main consequence of this characteristic is swirl and not uniform distribution of total pressure at the inlet of the compressor. This could potentially lead to unexpected stall and mechanical vibrations which can compromise the operational life of the entire propulsive system [2], [3]. Encouraging solution to this problem are mechanical vortex generators as proposed by Delot *et al.* [4] and active jets as proposed by Gissen *et al.* [5].

Multi objective optimization is another interesting method employed to this purpose. Nowadays CFD solver has allowed to study the flow field behavior throughout a duct with accuracy in a relatively short time. Thanks to this, an optimization algorithm can be employed to deform the geometry of an S-Duct. In this way, it is possible to search for the best configuration which reduce flow unsteadiness and distortion.

2. State of the art

In recent works [6,13] free-form deformation method coupled with multi-objective genetic algorithm was employed to improve aerodynamic characteristic in a diffusing S-Duct. The aim

36 of this work was the reduction of flow distortion and pressure losses through optimization of the
 37 intake shape by means of CFD. In Fig. 1 it is explained the optimization loop implemented in these
 38 works.

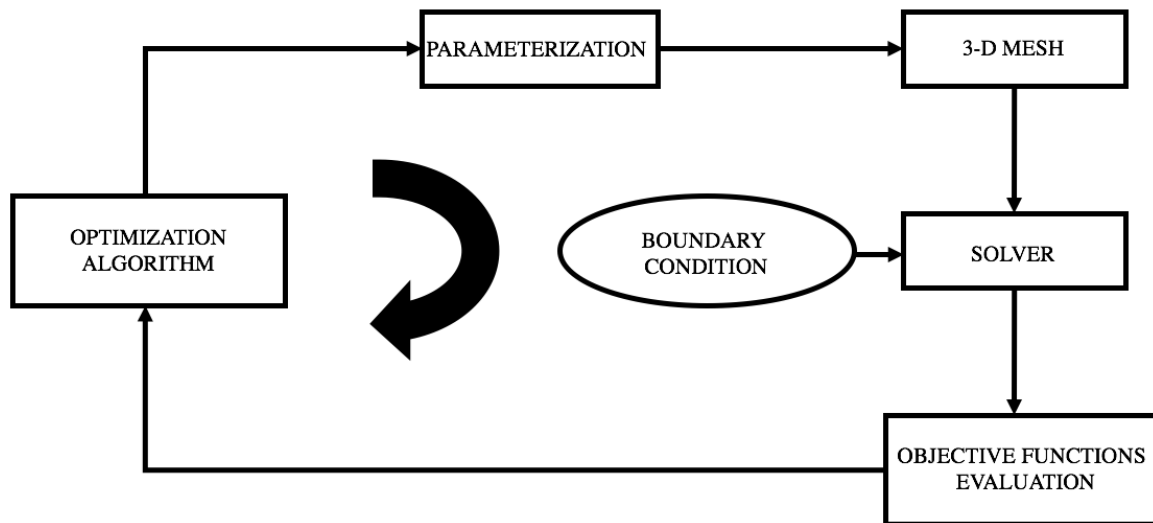


Figure 1. Optimization loop.

39 As baseline was chosen a known geometry experimentally [4,7,14,15] and numerically [16,17]
 40 investigated in previous works. The deformation of the geometry was performed implementing the
 41 FFD method. This provides for the creation of a parallelepipedic lattice which enclose the entire duct.
 42 The lattice nodes are named control points since their movement in space lead to deformations in the
 43 duct shape. Both in [6] and [13] were employed the same parameterization with a total of 80 control
 44 points and 240 degrees of freedom.

45 The rapid increase in computer computational speed makes these kind of studies possible.
 46 However to obtain good results from a CFD simulation of a 3D S-Duct, the computational time
 47 required is still relatively high and perform an optimization process with 240 degrees of freedom is
 48 impractical. For that reason, in addition to geometrical and manufacturing constraint, some other
 49 precautions has been taken into account and the number of degrees of freedom reduced to 36.

50 To evaluate the duct aerodynamic characteristic, total pressure leakage—described by the pressure
 51 coefficient (CP)—and swirl angle (α) at the aerodynamic interface plane (AIP) where taken into account.
 52 This two parameters are considered the ones that most influence the flow uniformity at the AIP.

53 The optimization algorithm adopted is the brain of this loop. Its task consist to evaluate the
 54 objective functions obtained from CFD simulations and change the position of control points leading
 55 to a new configuration of the duct. The modalities and the extent of these movements is what
 56 distinguishes the quality of a given optimization algorithm.

57 There are several different type of optimization algorithm. In [6] the Non-dominated Sorted
 58 Genetic Algorithm [18] was employed. The Pareto front obtained after 360 evaluations shows a
 59 maximum total pressure losses reduction of 20% and a maximum swirl reduction of 10% (Tab. 1). In
 60 [13] the Genetic Diversity Evolutionary Algorithm [19,20] was employed. The Pareto front obtained
 61 after 348 evaluations shows a maximum total pressure losses reduction of 24% and a maximum swirl
 62 reduction of 19% (Tab. 2). Both of this works employ an S-Duct of circular shape.

Table 1. Pareto front obtained with NSGA-II after 360 evaluations.

Individual	CP	α [deg]
Baseline	0.0310	3.3978
Best CP	0.0251	3.3657
Best swirl	0.0267	2.9764
Trade-off	0.0251	3.2827

Table 2. Pareto front obtained with GEDEA-II after 348 evaluations.

Individual	CP	α [deg]
Baseline	0.0315	3.4100
Best swirl	0.0302	2.7500
Trade-off	0.0239	2.8200
Trade-off	0.0288	2.7700
Best CP	0.0237	3.4200

In order to compare the results obtained from different algorithm, in this work we implemented the same optimization loop employing the Multi Objective Tabu Search algorithm [12]. Same baseline geometry was adopted and shape deformations were still performed with FFD method. However, differently from the works above mentioned, a new duct parameterization was implemented allowing a more intuitive and accurate deformation, employing the same number of control points. For CFD simulations RANS equation with $k - \omega$ SST turbulence model were adopted to simulate flow field. Performance of the S-Duct were evaluated in terms of pressure losses and stream-wise vorticity.

3. Methods

3.1. Baseline geometry configuration

The geometrical model implemented as baseline configuration was designed as defined in Wellborn et al [7]. The duct centerline is defined by two planar circular arcs with same radii, R , and subtended angles, $\theta_{max}/2$. Its coordinates are defined by the following equations:

For $0 \leq \theta \leq \theta_{max}/2$

$$x_{cl} = R \sin \theta \quad (1)$$

$$y_{cl} = R \cos \theta - R \quad (2)$$

$$z_{cl} = 0 \quad (3)$$

For $\theta_{max}/2 \leq \theta \leq \theta_{max}$

$$x_{cl} = 2R \sin \theta - R \sin \theta_{max} - \theta \quad (4)$$

$$y_{cl} = 2R \cos \theta - R - R \cos \theta_{max} - \theta \quad (5)$$

$$z_{cl} = 0 \quad (6)$$

All cross-section perpendicular to the centerline were circular with radius defined as follow:

$$\frac{r}{r_1} = 1 + 3 \left(\frac{r_2}{r_1} - 1 \right) \left(\frac{\theta}{\theta_{max}} \right)^2 - 2 \left(\frac{r_2}{r_1} - 1 \right) \left(\frac{\theta}{\theta_{max}} \right)^3 \quad (7)$$

where r_1 and r_2 are the inlet and the outlet radius respectively. Both centerline and radius distribution are a function of the arc angle θ .

In order to validate our flow simulation result, we chose the same parameters adopted by Delot [9] as described in Tab. 3.

Table 3. S-Duct baseline geometry parameters

Parameter	Value
θ_{max}	60°
R	$0.6650m$
r_1	$0.0665m$
r_2	$0.0820m$

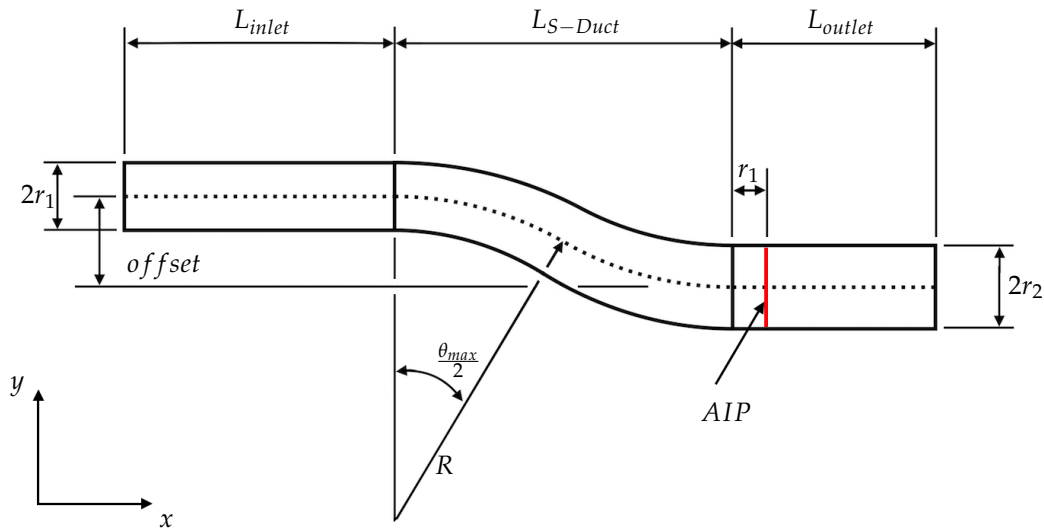
80 Fig. 2 represent a section of the overall baseline geometry in the $x - y$ plane which is a symmetry
81 plane for the duct. To obtain more accurate results, we introduced two additional parts:

- 82 • at the inlet, a cylindrical duct eight times longer than the inlet radius. Its purpose is to ensure
83 uniform inlet conditions;
- 84 • at the outlet, a cylindrical duct six times longer than the outlet radius. Its purpose is to guarantee
85 that the outlet conditions do not have any influence on the upstream flow.

86 All the flow distortion parameters are evaluated at a cross-sectional plane, the AIP, located
87 downstream the outlet as explained in Fig. 2 and Tab. 4.

Table 4. Overall geometry parameters

Parameter	Values
<i>Offset</i>	$2R(1 - \cos(\theta_{max}/2))$
L_{S-Duct}	R
L_{inlet}	$8r_1$
L_{outlet}	$6r_1$
$L_{AIP} = L_{inlet} + L_{S-Duct} + r_1$	$9r_1 + R$
$L_{TOT} = L_{inlet} + L_{S-Duct} + L_{outlet}$	$14r_1 + R$

**Figure 2.** S-Duct scheme.

88 3.2. Geometry parameterization

89 Since the main target of this work is the optimization of an S-Duct, the description of the
90 entire geometry with a flexible and simple method becomes of crucial importance. Purpose of
91 parameterization is reduce the number of geometric parameters (decision variables) necessary to
92 draw the geometry, which translates into a reduction of the overall optimization computational cost.
93 Furthermore, parameterization should also allows an efficient modification of the shape of the S-Duct.

FFD [10] is the method employed to parameterize and deform the baseline geometry. It consists of embedding the considered geometry into a 3D parallelepipedic lattice regularly subdivided which nodes are called control point. The position of each point in the considered geometry is described by a weighted sum of the control points position. We implemented this method adopting the following simplification:

- since our S-Duct is symmetric with respect to the $x - y$ plane, we decided to design and simulate only half of the duct in order to reduce the computational cost;
- we consider the cylindrical ducts added after and before the S-Duct of fixed geometry, as manufacturing constraints. This means that the only part that have to be parameterized is the S-Duct itself.

Since there is nothing inside the duct (the mesh will be created in a later time), the entire geometry can be described only by the external surface. Therefore a 2D lattice can be adopted. For that reason, the best position for the control point would be on the surface of the S-Duct. Following that reasoning, l equally spaced semicircular cross-section perpendicular to the centerline can be defined. On each of them we can define m equally spaced control point.

However this solution does not represent a parallelepipedic lattice, or rather, it represents it but only in a local system of reference integral with the surface. A possible solution can be define a transformation of coordinate from the Cartesian system of reference to the new one. Here perform the FFD and in the end define a second transformation of coordinate that bring back to the Cartesian reference the deformed geometry.

This method is accurate and precise, but complex to the point of increasing the overall computational cost. To overcome this problem, we implemented a similar and simpler solution. We considered a planar rectangular surface, as in Fig. 3, on which we could easily defined a parallelepipedic lattice.

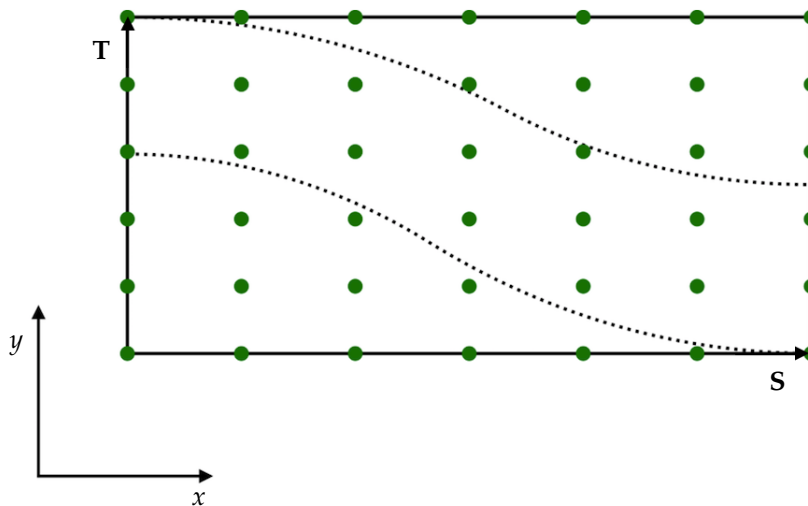


Figure 3. Parallelepipedic lattice defined on a plane surface in the symmetry plane (plane $x - y$) of the S-Duct. Dotted lines represent the duct projection on this plane: that curves define the main lattice dimensions

In this case the FFD is mathematically described by the following equation:

$$X_{ffd} = \sum_{i,j=0}^{l,m} B_i(s)B_j(t)P_{ij} \quad (8)$$

118 where:

- 119 • X_{ffd} is a vector containing the Cartesian coordinates of the displaced point;
- 120 • l, m are the number of control point in S and T direction respectively;
- 121 • $B_k(u)$ are the degree 3 Bernstein polynomials;
- 122 • s, t are the generic point coordinate in the $S - T$ system of reference ($0 \leq s \leq 1, 0 \leq t \leq 1$);
- 123 • P_{ij} is a vector containing the Cartesian coordinates of the control point.

124 If now we move every control points of a fixed S to a cross-section, perpendicular to the centerline,
 125 in the baseline geometry as described above (see Fig. 4) and then we perform the FFD on the plane
 126 surface, what we obtain is a result similar to baseline geometry.

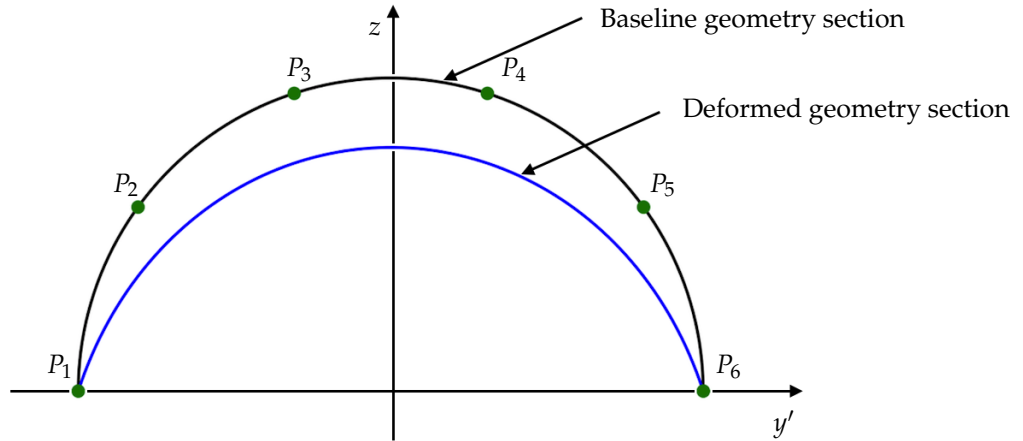


Figure 4. Generic-cross section. Black semicircular line represent the baseline geometry. The blue line represent the deformed geometry when the control points $P_1 - P_6$ are equally spaced on the baseline geometry section.

127 The main problem of this solution is that the control points do not interpolate the surface, but
 128 they are only close to it. To obtain a closer result, we modified the control points position as follow:

1. In every cross-section, the deformed geometry is described by a Bezier curve, that is a 1D formulation of the 2D initial FFD problem:

$$X_{ffd} = \sum_{i=0}^m B_j(t)P_i \quad (9)$$

129 Fixed $m = 6$, we inverted this equation in order to find the control points position that correctly
 130 interpolate a semicircle. To do this, we imposed the following constraints:

- 131 • $y'_{P_1} = -r$
- 132 • $y'_{P_1} = y'_{P_2}$: tangency condition
- 133 • $z_{P_3} = z_{P_4}$: symmetry condition
- 134 • $z_{P_2} = z_{P_5}$: symmetry condition
- 135 • $y'_{P_3} = -y'_{P_4}$: symmetry condition
- 136 • $y'_{P_5} = y'_{P_6}$: tangency condition
- 137 • $y'_{P_6} = r$

where r is the semicircle radius in the particular cross-section. After some calculations we obtained:

$$z_{P_2} = z_{P_5} = r \frac{4(8\sqrt{2} - 9)}{15} \quad (10)$$

$$z_{P_3} = z_{P_4} = r \frac{2(21 - 8\sqrt{2})}{15} \quad (11)$$

$$y'_{P_3} = -y'_{P_4} = r \frac{2(64\sqrt{2} - 79)}{45} \quad (12)$$

$$(13)$$

138 2. In order to guarantee tangential condition at the inlet and at the outlet, the control points in the
139 inlet section are copied and translated shortly after. The control points in the outlet section are
140 copied and translated shortly before.

141 In previous works [6] the parameterization of the same baseline geometry were performed with a
142 3D parallelepipedic lattice. This solution allows to recreate a precise baseline geometry. However, since
143 our final purpose is to deform the S-Duct geometry, starting from a slightly different shape wont affect
144 the final result. Furthermore our solution allowed us to modify the duct geometry more efficiently and
145 accurately since all the control points lie near the duct surface.

146 The degrees of freedom (dof) of our new parameterization can be defined as follow:

- 147 • The control point in the first two cross-section from the S-Duct inlet and the last two before the
148 outlet are fixed. This is due to manufacturing constraints.
- 149 • Referring to Fig. 4, in every other cross-section we have:
 - 150 – Point on the symmetry plane (P_1, P_6) can only move on the symmetry plane ($dof_{P_1} = 2,$
151 $dof_{P_2} = 2$).
 - 152 – To maintain tangency condition, point P_2 and P_5 have the same x and y coordinates as P_1
153 and P_6 respectively. They can move in z - direction ($dof_{P_2} = 1, dof_{P_5} = 1$).
 - 154 – point P_4 and P_3 can move in the space ($dof_{P_3} = 3, dof_{P_4} = 3$).

155 This means that every cross-section have 12 dof. In previous work [6], 36 dof were imposed.
156 Therefore to maintain the same number, three cross-section between the two fixed section at the inlet
157 and outlet were imposed in our parameterization ($l = 7$).

158 3.3. S-Duct Performance metrics for the optimization

159 In this work a multi-objective optimization was performed. Two objective functions were
160 considered to quantify the S-Duct performance during the optimization process:

1. $f_1 = 1 - \overline{PR}$ (14)

$$f_1 = 1 - \overline{PR} \quad (14)$$

which describe the pressure coefficient CP while PR represent the non dimensional area-averaged total pressure recovery:

$$PR = \frac{p_{0,AIP}}{p_{0,inlet}} \quad (15)$$

2. $f_2 = |\bar{\alpha}|$ (16)

$$f_2 = |\bar{\alpha}| \quad (16)$$

where α represent the swirl angle i.e. the ratio between the tangential and the axial components of the velocity vector. It is defined as follow:

$$\alpha = \arctan \left(\frac{V_{\theta,AIP}}{V_{x,AIP}} \right) \quad (17)$$

Tangential velocity has been calculated as:

$$V_{\theta} = \sqrt{V_y^2 + V_z^2} \quad (18)$$

161 Even if arctan is an odd function, in this case we can neglect the sign of its arguments—i.e. the sign of
162 V_{θ} —since we are only interested in the swirl angle absolute value.

163 Both objective functions were evaluated in the barycenter of each mesh cells at the AIP. Then the
164 global value was defined through an area-average integral.

165 3.4. Optimization method

166 To minimize pressure losses and swirl angle we interfaced our parameterization with *Nimrod/O*,
167 an open source tool for distributed optimization [11]. This tool gave us the possibility to choose among
168 different optimization methods and in particular we chose the Multi-Objective Tabu Search-2 (MOTS2)
169 based on the MOTS algorithm described in Jaeggi *et al.* [12].

170 All the 36 parameters described above are free to move inside a parallelepipedic box that enclose
171 the S-Duct:

- 172 • x -direction: between S-Duct inlet and outlet
- 173 • y -direction: $[-10.5r_1, 9r_1]$
- 174 • z -direction: $[-4.5r_1, 9r_1]$

175 In addition to the parameterization constraints, the following were defined in order to avoid unfeasible
176 geometry during optimization:

- for line upper (UP) and lower (DW) curves in the symmetry plane:

$$y_{UP}(x) > y_{DW}(x) \quad (19)$$

- Referring for simplicity to the generic cross-section in Fig. 4, if $y_{P_4} < y_{P_3}$:

$$y_{P_4} - y_{P_3} < r1 \quad (20)$$

- with $X_{P_j}[i]$ we indicate the j control point x -range in the generic i cross-section:

$$X_{P_j}[i-2] \leq X_{P_j}[i] \leq X_{P_j}[i+2] \quad (21)$$

177 3.5. Computational method

178 3.5.1. Flow simulation

179 The objective functions of every deformed ducts were evaluated from the result of a
180 pressure-based steady-state RANS simulation. In [8] the performance of different turbulence models
181 for the RANS simulation of the flow in the same S-Duct studied by Wellborn *et al.* [8] are compared.
182 The four equation transition SST model provided the best match with the experimental data. However
183 due to the high computational cost associated with this model, the $K - \omega$ SST model was adopted for
184 further investigations since it provided similar results at a reasonable computational cost. Therefore,
185 for our work $K - \omega$ SST model was set up. As explained in next sections, simulation results has been
186 validated comparing them with experimental results showed in [9].

187 During optimization, simulations were carried out running the first 200 iterations with the first
188 order of solution accuracy for all the flow parameters. For the other 500 iteration all the parameters
189 were set to the second order. A total of 700 iterations was performed in order to have every residual
190 around 10^{-5} .

3.5.2. Mesh generation

To choose the appropriate mesh for our simulations, we created a series of different meshes for the same topology used in [9]. The differences among these meshes are in terms of number of mesh element, first layer thickness and growing rate. In this way we wanted to find the best mesh parameters combination which reproduces experimental result in [9].

In Fig. 5a is represented this comparison: as we increase the number of mesh cells, PR is getting closer and closer to the experimental result. For a number of mesh elements higher than 1.7 million the numerical results seem to start to oscillate around an average value. Similar behavior can be found in Fig. 5b for the swirl.

Thanks to these results, we chose the mesh showing the closer behavior to the experimental results. For every new geometry a structured mesh of around $1.8 \cdot 10^6$ nodes was generated. Every mesh shares the same general properties in order to guarantee comparable results. An H-grid structure was imposed in the center of the duct section and an O-grid structure around the walls (Fig. 6).

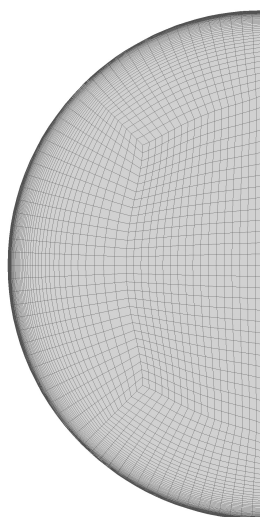


Figure 5. Cross-section mesh topology.

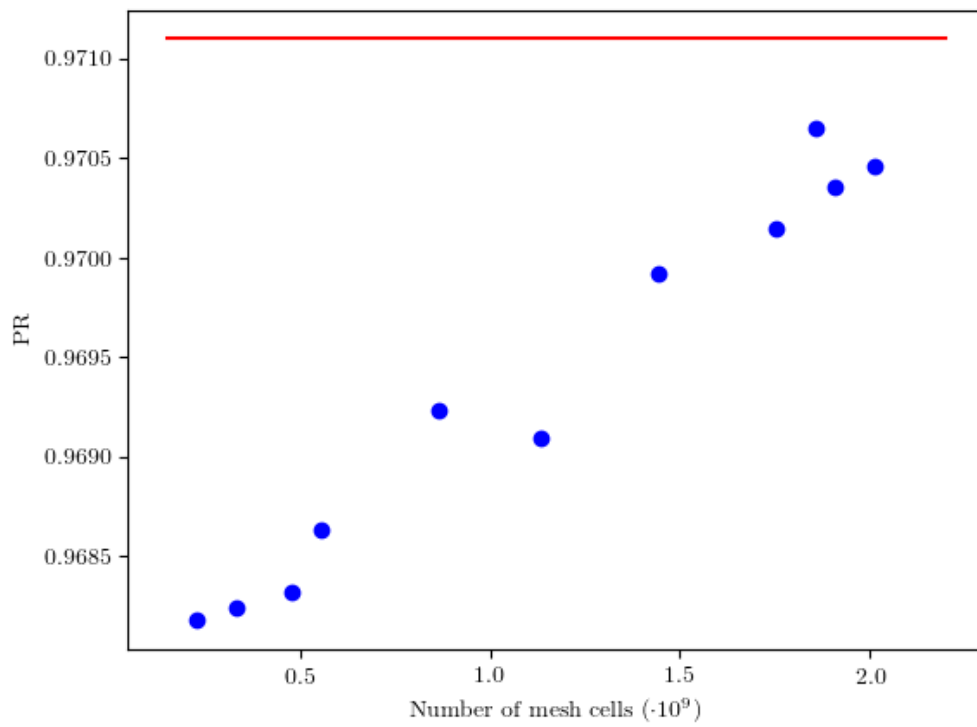
The first layer thickness on the wall was imposed to ensure that the y^+ would be smaller than 1 over the full domain: with a first layer thickness of $2 \cdot 10^{-6}$ we obtained a maximum y^+ of about 0.8. The expansion ratio from the wall was set equal to 1.05. The number of nodes in each cross-section is approximately 6000, while the number of cross-sections is 360.

3.5.3. Boundary conditions

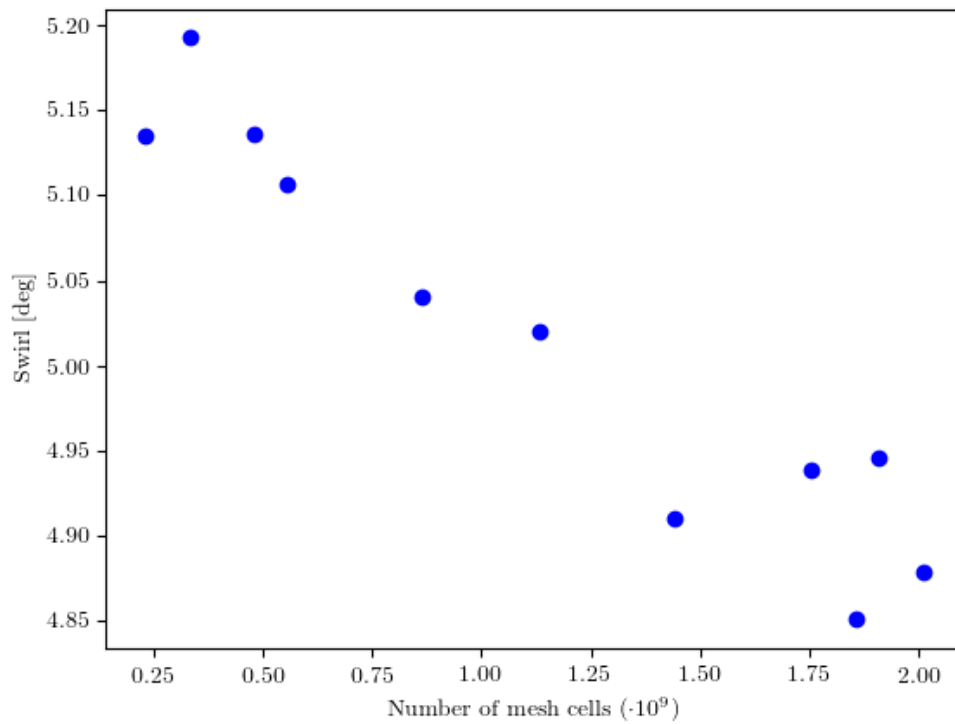
Boundary conditions were applied to match the experimental condition described in [9] and collected in Tab. 5.

Table 5. Boundary conditions for the simulations

Parameter	Value
Inlet total pressure	88744Pa
Inlet static pressure	69575Pa
Outlet static pressure	78982Pa
Total temperature	286.2K



(a)



(b)

Figure 6. (a) PR and (b) swirl angle as a function of the number of mesh elements. The red solid line in (a) represent the experimental result form [9].

211 4. Results

212 4.1. Baseline analysis

213 In the previous section we used experimental results and in particular the area averaged
 214 pressure recovery at AIP as a reference point in order to choose the mesh with the most appropriate
 215 characteristics. In this subsection we will investigate these results more in depth in order to validate the
 216 baseline geometry used as optimization starting point. In Fig. 7 it is shown the AIP pressure recovery
 217 in three different situations. In (a) we have the experiment carried out by Delot [9]. In (b) we have
 218 our numerical results obtained for an exact copy of the geometry used by Delot. In (c) we have our
 219 numerical results obtained reproducing the baseline geometry employing our new parameterization.

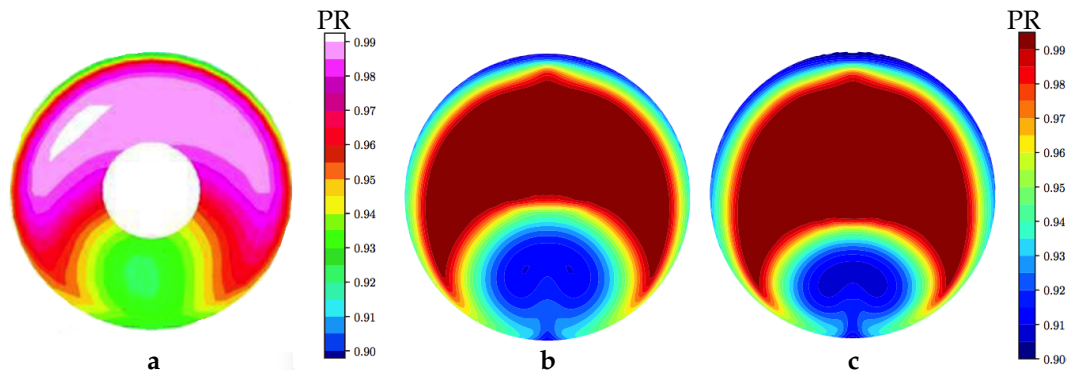


Figure 7. Baseline pressure recovery comparison: (a) Delot Experiment [9], (b) CFD simulation with same geometry, (c) CFD simulation with geometry obtained from our new parameterization.

220 Similar behavior can be detected in all the three images which confirm a coherent behavior
 221 between simulations and experiment. In Tab. 6 we can compare the area averaged pressure recovery
 222 in the three cases. As expected, we obtained almost the same PR in all the three cases and in particular
 223 the percentage error between baseline (a) and (b) is only 0.0515%. It is interesting to note how the
 224 baseline (c) shows an increase of about 0.1% in PR and a reduction of about 11.1% in Swirl with respect
 225 to baseline (b). This means that the baseline geometry obtained with our new parameterization is
 226 already itself an optimized solution. For that reason, to compare our final optimized results, we will
 227 use baseline (b) since it is the closest result to Delot experiment in terms of geometry.

Table 6. S-Duct performance in baselines geometry : (a) Delot Experiment [9], (b) CFD simulation with same geometry, (c) CFD simulation with geometry obtained from our new parameterization.

	PR	Swirl [deg]
Baseline (a)	0.9711	
Baseline (b)	0.9706	4.8511
Baseline (c)	0.9715	4.3540

228 4.2. Results from the optimization process

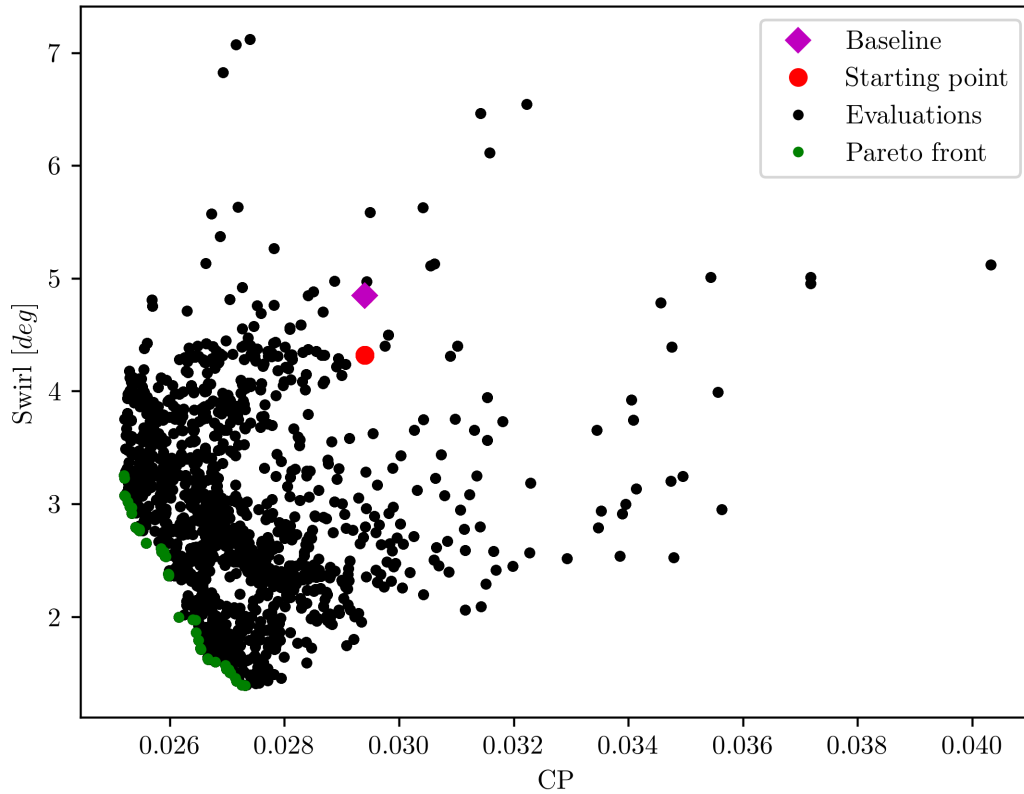


Figure 8. The Pareto front and the history of the optimization study.

229 The final results of our optimization are outlined in Fig. 8. The baseline objective functions are
 230 indicated with a violet diamond. As already said, this is not the optimization starting point which
 231 instead is represented by a red dot. This point represent the value of the objective function of the
 232 geometry obtained employing our new parameterization. We performed a total of 1300 evaluations
 233 which produced the Pareto front highlighted by the green dots. This result however shows some
 234 discontinuity in the Pareto front which means that not all the design space has been explored and more
 235 evaluations are needed.

236 Despite this, our optimization already shows remarkable results as enlighten in Tab. 7 in which
 237 there are collected the objective functions value for the two extreme point and some trade-off solutions
 238 on the Pareto front. The solution with minimal total pressure losses is named opt_{CP} and shows a
 239 reduction of about 14.3% compared to the baseline geometry. The solution with minimal swirl is
 240 named opt_{α} and shows a reduction of about 70.9% compared to the baseline geometry. The trade off
 241 solution are named opt_1 , opt_2 and opt_3 and they are the point on the border of the main discontinuity
 242 in the Pareto front. opt_1 and opt_2 have similar CP but different swirl angle; opt_2 and opt_3 instead has
 243 similar swirl angle and different CP.

Table 7. Objective functions comparison between the Baseline geometry, the extreme point and three trade-off solutions in the Pareto front.

	<i>CP</i>	Improvement	Swirl [<i>deg</i>]	Improvement
Baseline (b)	0.0294		4.8511	
<i>opt_{CP}</i>	0.0252	14.3%	3.2560	32.9%
<i>opt₁</i>	0.0261	11.2%	2.5216	48.0%
<i>opt₂</i>	0.0262	10.9%	1.9972	58.8%
<i>opt₃</i>	0.0264	10.2%	1.9713	59.4%
<i>opt_α</i>	0.0275	6.5%	1.4109	70.9%

244 Analyzing the AIP distribution of total pressure we can see how in *opt_{CP}* (Fig. 9a) the low total
 245 pressure area near the lower duct portion has almost the same dimensions as the baseline, while
 246 the mean total pressure value has increased. However, a second and smaller low total pressure
 247 area appeared: its dimension is still small and its extension is confined near the external surface.
 248 Furthermore, we can see a general reduction in pressure losses near the external duct surface. If
 249 we consider now *opt_α* (Fig. 9b) we can see how this second area increase in dimension to the point
 250 of equaling the main area. The latter has considerably diminished its dimensions compared to the
 251 baseline, however the presence of this second low total pressure area frustrates any improvements.

252 To understand this behavior we have to compare the geometry of the optimized ducts. In Fig.
 253 10 there are a series of cross-section perpendicular to *x*-direction from *opt_{CP}* and *opt_α* showing total
 254 pressure contours. The appearance of the second low total pressure region we discuss earlier occurs
 255 in the second half part of the duct and its presence is relative to the particular shape that the duct
 256 assumes in the first half part: here *opt_{CP}* approaches a rectangular shape while *opt_α* approaches a
 257 triangular shape. From Fig. 11 we can see that in the first half part of the duct both *opt_{CP}* and *opt_α*
 258 has the same cross-section area, however its distribution is completely different. In *opt_{CP}* the area
 259 distribution is almost symmetrical with respect to *xz*-plane instead in *opt_α*, since the triangular shape,
 260 the area distribution is mainly concentrated in the upper half part of the duct. To satisfy the constraint
 261 of circular cross-section at the outlet, each ducts undergo a deformation in their second half part. In
 262 correspondence of this enlargement occurs a second boundary-layer separation (Fig. 12) which leads
 263 to the creation of the secondary lower total pressure region. This behavior is much more evident in
 264 *opt_α* since the transformation from triangular to circular shape in the lower part of the duct is much
 265 deeper and sudden.

266 In [21] a similar optimization was performed on a S-Duct with rectangular cross-section. The best
 267 solutions in terms of *CP* reduction show values smaller than 0.05. Even if our best *CP* is several times
 268 greater than this result, it is interesting to note how our optimization lead to find a best solution in
 269 terms of *CP* reduction characterized by a rectangular cross-section.

270 Fig. 13 illustrates the axial velocity distribution on the symmetry plane: here we can observe a
 271 significant shrinking of the separation bubble for all the optimal solutions compared to the baseline.
 272 Also in this case *opt_{CP}* and *opt_α* show two different behavior: while in the first case the separation
 273 region is restricted just after the first duct bent, in the second case we can see a long separation area
 274 which runs for all the S-Duct length. Despite this, it remains very narrow and adjacent to the wall.
 275 Same behavior is shown by *opt₂* and *opt₃*, while *opt₁* is much similar to *opt_{CP}*.

276 The size of the separation bubble is quantified from the distribution of the *x*-component of the
 277 wall shear stress on the duct wall. The length of the recirculation region is calculated as the axial length
 278 for which we detected a negative shear stress, as outlined in Fig. 14. The baseline geometry shows a
 279 wide recirculation area located in the second half part of the duct. In *opt_{CP}* and *opt₁*, instead, we can
 280 observe a reduction on the axial velocity in the lower part of the duct: *opt_{CP}* shows only a small and
 281 very weak recirculation region in the first half part of the duct while *opt₁* shows no recirculation at all.
 282 High flow distortions are responsible for the low total pressure area in a S-Duct. However, even if *opt₁*
 283 doesn't show any recirculation area it isn't the best solution in terms of pressure losses reduction. This

284 is due to its cross-section shape that, like opt_{α} has, is triangular which means the presence of a second
285 low total pressure region.

286 For opt_2 , opt_3 and opt_{α} , instead, the recirculation area is clearly evident and it occurs in the
287 initial/central part of the duct upstream of where it occurs in the baseline. Furthermore opt_3 and opt_{α}
288 show a secondary and weaker recirculation region towards the end of the S-Duct. Despite this, the
289 separation region remains always very narrow and close to the duct lower wall. This behavior comes
290 from two different geometric factors. The first is the ducts profile on the symmetry plane: the lower
291 curve starts with a strong and fast downward bent followed by a constant slope section that ends at the
292 outlet fitting (Fig. 15). This are the reason of the early separation in comparison with the baseline. The
293 second is the cross-section area distribution: unlike the baseline and opt_{CP} , all the other ducts present
294 a first fast increase in the cross-section area followed by a local minimum and a second fast increase
295 (Fig. 11) characterized by a similar slope as the first part. This means that at about three quarter of
296 these ducts there is a gauge as highlighted also by the upper line in the symmetry plane section (Fig.
297 15). This gauge force the flow to increase its velocity and, in particular, to decrease its static pressure
298 through it.

299 To better understand this last statement we have to consider Fig. 16 in which are represented the
300 static pressure profile in different cross-section of opt_{CP} and opt_{α} . As already experimentally observed
301 in Wellborn *et al* [3,7], opt_{CP} shows an inversion in the pressure gradient direction about halfway along
302 the length of the duct. This explain why in this geometry (together with the baseline and opt_1) the
303 separation region is pushed towards the upper wall continuing to increase its size. In opt_{α} instead,
304 static pressure is almost constant in the first half part of the duct and a weaker pressure gradient with
305 respect to opt_{CP} appears only in the second half part. Same behavior is shown by opt_2 and opt_3 . This
306 explains both the long narrow separation region and the second separation region in opt_3 and opt_{α} .

307 The swirl reduction is the main achievement of this numerical simulation. In fact, in opt_{α} we
308 obtained a impressive reduction of mean swirl angle of about 70% at the AIP. Here the swirl angle has
309 a maximum value of $7.9[deg]$, almost one third with respect to the baseline ($24.3[deg]$). If we consider
310 the contour plot at the AIP (Fig. 17) we can see how α differs from zero only in the lower part of the
311 duct. Furthermore opt_{CP} , even if it represent the worst solution in terms of swirl angle reduction,
312 shows a substantial improvement of about 30%. Remembering the definition of swirl angle (Eq. 17), to
313 explain this achievement we have to analyze the axial and tangential velocity distribution: all depends
314 on the ratio of this two quantities at the AIP. In Fig. 13 it is represented the axial velocity profile in
315 different cross-section of opt_{PC} and opt_{α} . At the AIP we can observe a similar velocity distribution
316 with the exception of presence of the second low total pressure area in the first half part of opt_{α} . For
317 that reason swirl angle is strongly linked to tangential velocity distribution.

318 In Fig. 18 it is represented the absolute value of tangential velocity profile in different cross-section
319 of opt_{PC} and opt_{α} . At the AIP the tangential velocity is close to zero in the upper part of both duct.
320 The lower part instead, is characterized by higher values due to the separation region. Here we can in
321 fact distinguish two regions of high tangential velocity just in correspondence to the two separation
322 region, one on the symmetry plane and one near the external wall. The extreme low tangential velocity
323 value in opt_{α} is, also in this case, linked to the particular triangular shape of this duct. As already said,
324 the strong area increase in the ending and lower part of the duct due to the transition from triangular
325 to circular cross-section implement the diffusing duct characteristic leading to an increase in static
326 pressure and a strong reduction in tangential velocity.

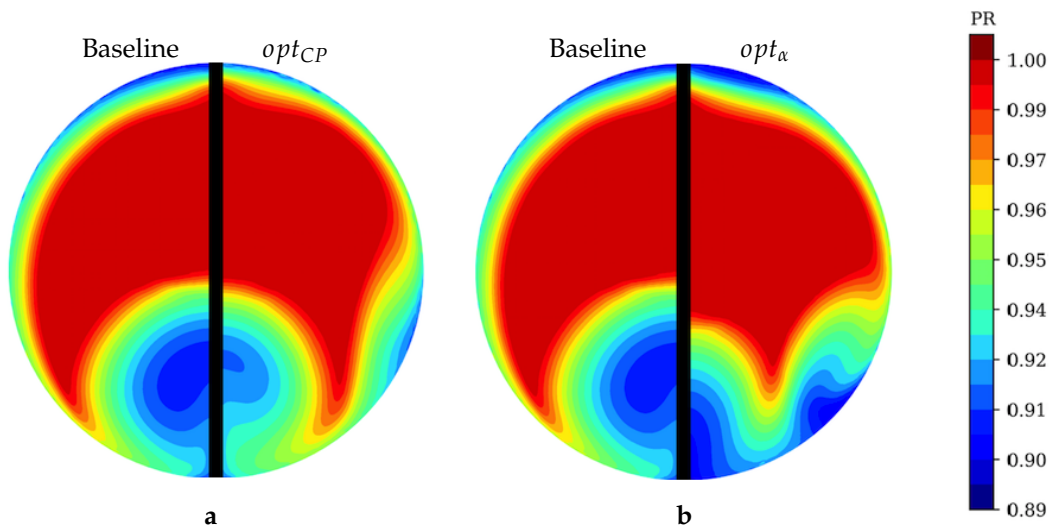


Figure 9. Total pressure distribution at AIP. (a) Comparison between Baseline and opt_{CP} . (b) Comparison between Baseline and opt_{α} .

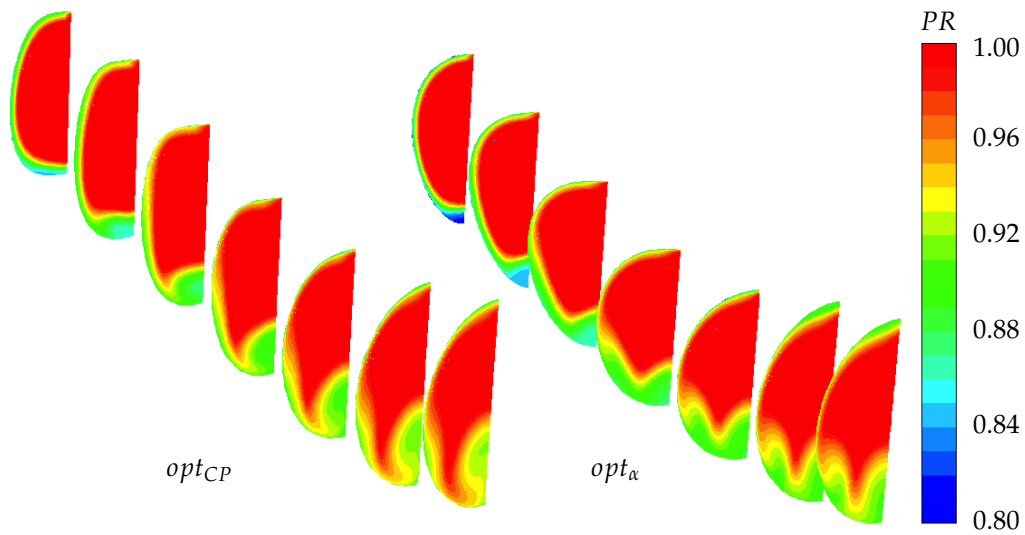


Figure 10. Total pressure distribution in different cross-section: comparison between opt_{CP} (left) and opt_{α} (right). Every cross-section is perpendicular to x -direction and situated at $x = 2.5r_1$, $x = 4r_1$, $x = 5.5r_1$, $x = 7r_1$, $x = 8.5r_1$, $x = 10r_1$ (S-Duct outlet) and $x = 11r_1$ (AIP) from S-Duct inlet.

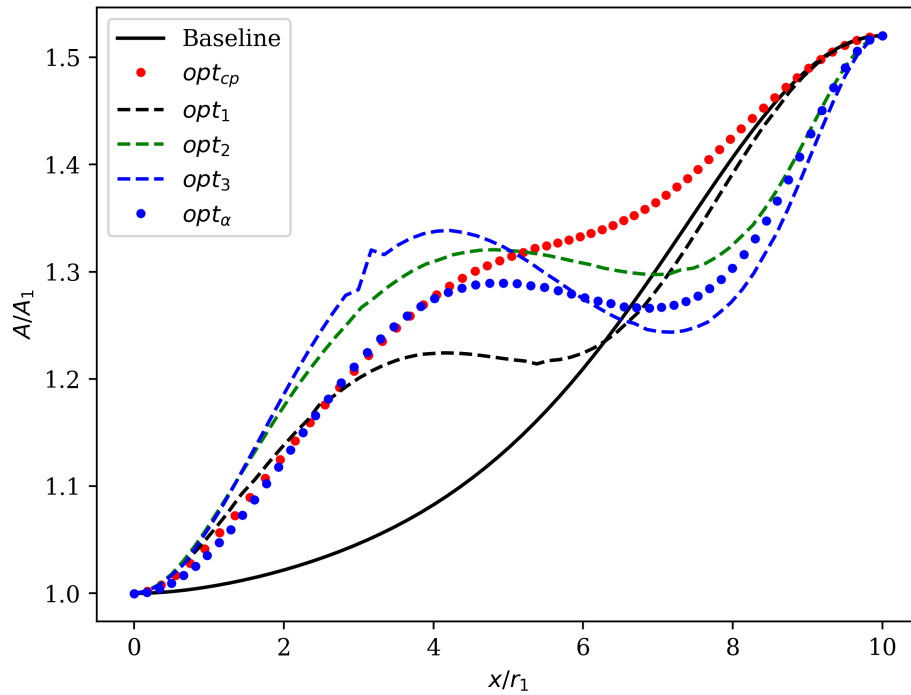


Figure 11. S-Duct cross-sections area in optimized solutions compared with Baseline. y -axis represent the ration between the area of the generic cross-section perpendicular to x -direction and inlet area.

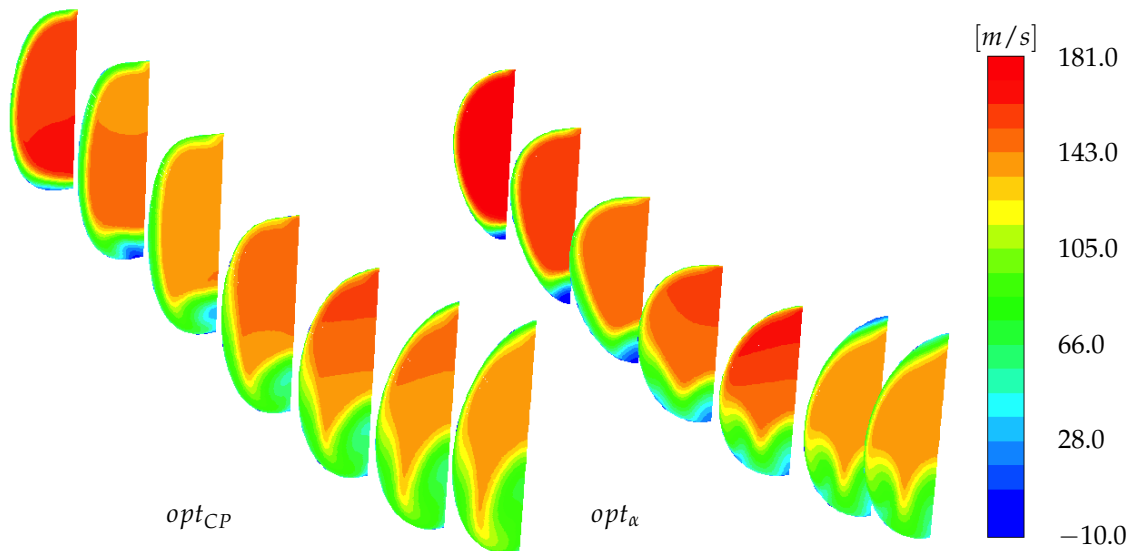


Figure 12. Axial velocity distribution in different cross-section: comparison between opt_{CP} (left) and opt_{α} (right). Every cross-section is perpendicular to x -direction and situated at $x = 2.5r_1$, $x = 4r_1$, $x = 5.5r_1$, $x = 7r_1$, $x = 8.5r_1$, $x = 10r_1$ (S-Duct outlet) and $x = 11r_1$ (AIP) from S-Duct inlet.

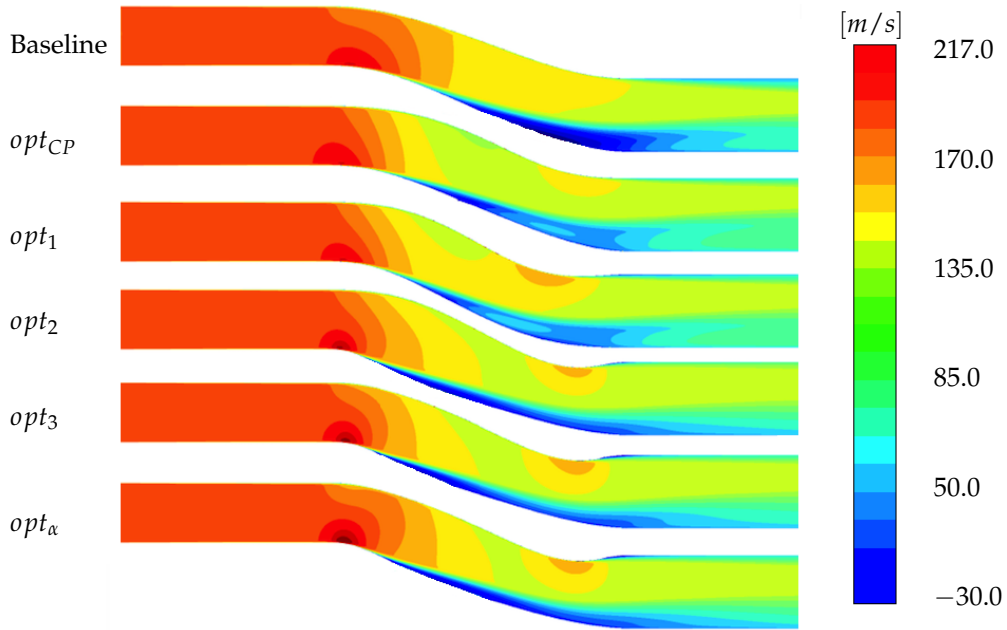


Figure 13. Axial velocity distribution on symmetry plane in optimized solutions compared with Baseline.

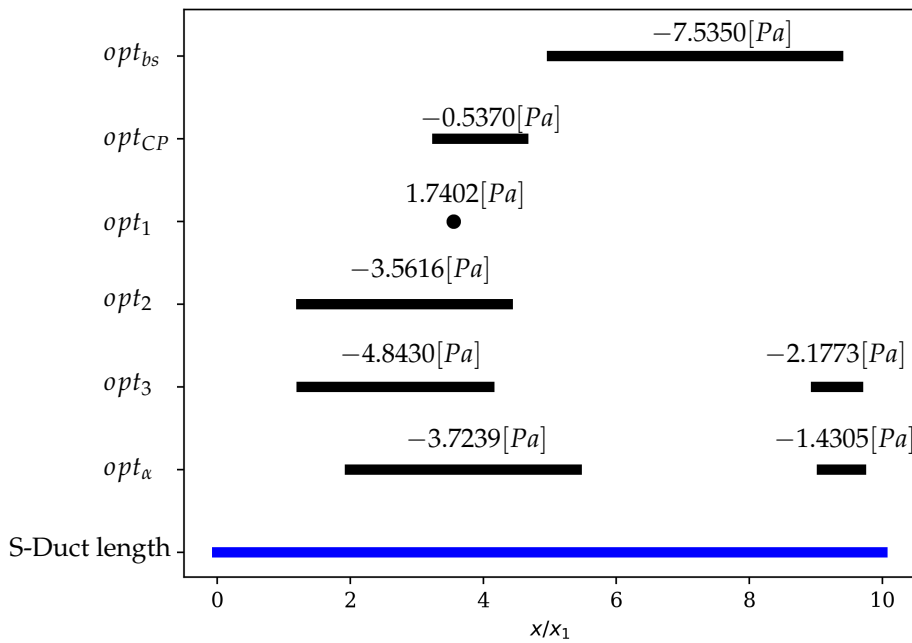


Figure 14. Recirculation region in optimized solutions compared with Baseline. Blue line represent the total S-Duct axial length. Black lines represent the axial length of recirculation region. Numbers over each lines states the minimum values of x -wall shear stress. Black dot in correspondence of opt_1 indicates the position of the minimum (positive) value of x -wall shear stress for that geometry.

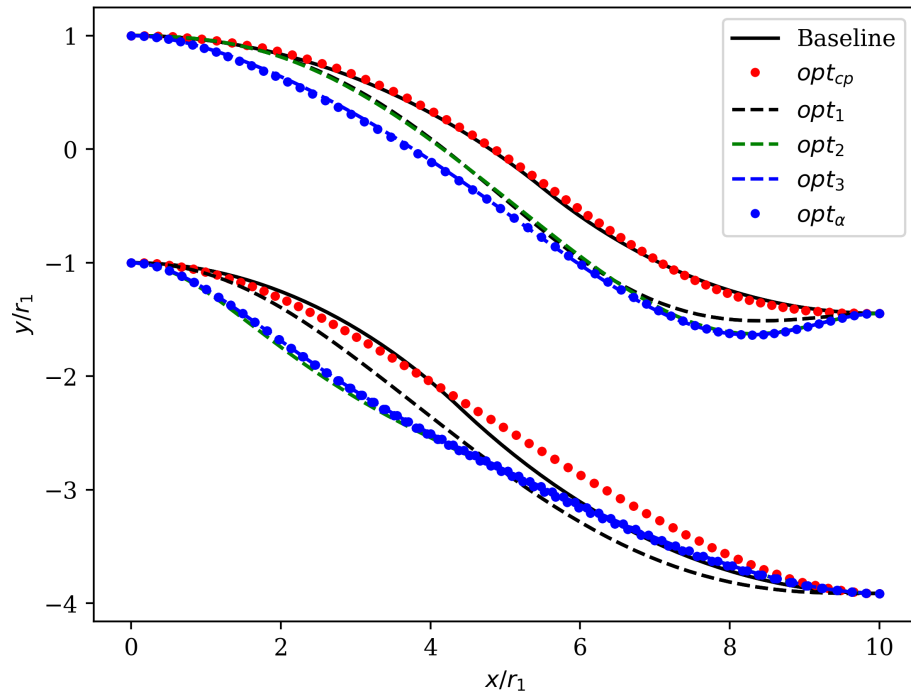


Figure 15. S-Duct geometry on symmetry plane in optimized solutions compared with Baseline.

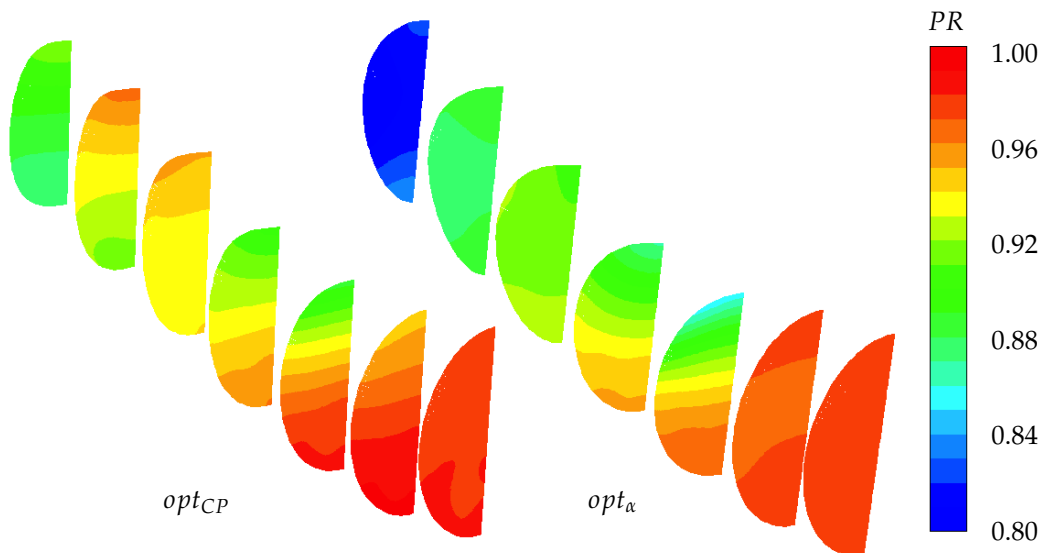


Figure 16. Static pressure distribution in different cross-section: comparison between opt_{CP} (left) and opt_{α} (right). Every cross-section is perpendicular to x -direction and situated at $x = 2.5r_1$, $x = 4r_1$, $x = 5.5r_1$, $x = 7r_1$, $x = 8.5r_1$, $x = 10r_1$ (S-Duct outlet) and $x = 11r_1$ (AIP) from S-Duct inlet.

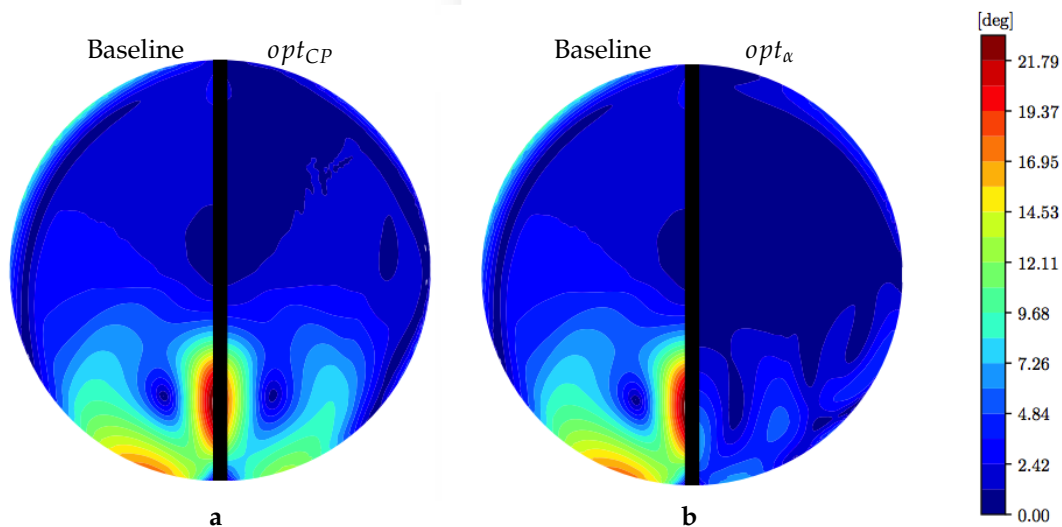


Figure 17. Swirl angle distribution at AIP. (a) Comparison between Baseline and opt_{CP} . (b) Comparison between Baseline and opt_{α} .

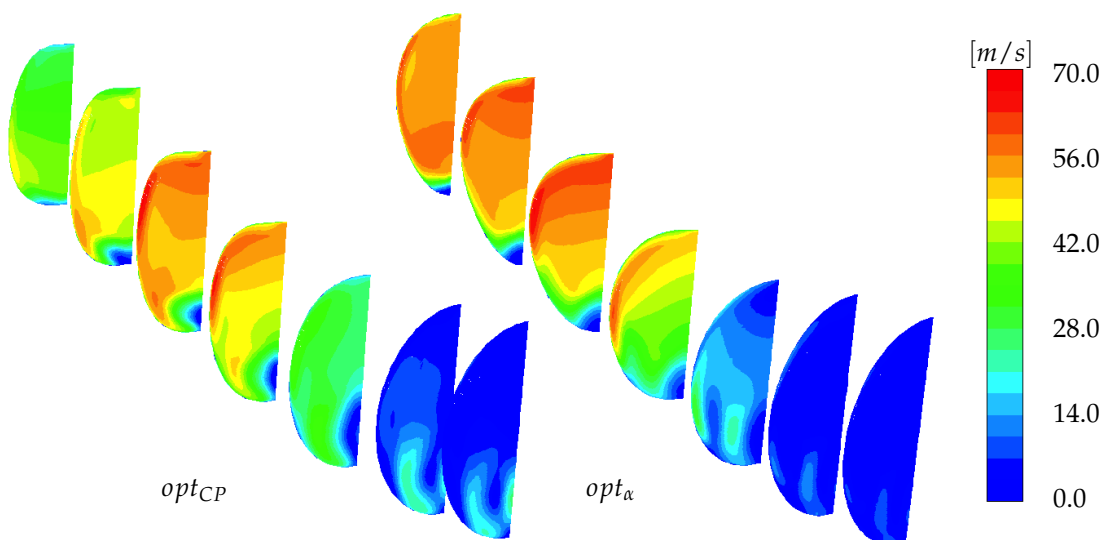


Figure 18. Absolute value of tangential velocity distribution in different cross-section: comparison between opt_{CP} (left) and opt_{α} (right). Every cross-section is perpendicular to x -direction and situated at $x = 2.5r_1$, $x = 4r_1$, $x = 5.5r_1$, $x = 7r_1$, $x = 8.5r_1$, $x = 10r_1$ (S-Duct outlet) and $x = 11r_1$ (AIP) from S-Duct inlet.

327 4.3. Multidimensional data analysis of the optimization process

328 In addition to the flow analyses we performed an analysis of the whole design space of
 329 the optimization problem. This requires the simultaneous visualization of the design parameters
 330 and objective functions, which results in 38 dimensions. We use Parallel Coordinates [22] for the
 331 visualization of the multidimensional space, and the interactive approach as initially proposed in [23]
 332 and expanded in [24] for computational engineering design data.

333 In Fig. 19 is presented the visualization of the whole history of the optimization study and a
 334 region close to the Pareto front is selected. The design parameter x_{23} exhibit a particular characteristic;
 335 high values reflect the compromise region, a specific value reflects the region for the lowest swirl, and
 336 lower value reflect the region for the lowest pressure losses. Fig. 20 shows the three different selections
 337 for x_{23} values.

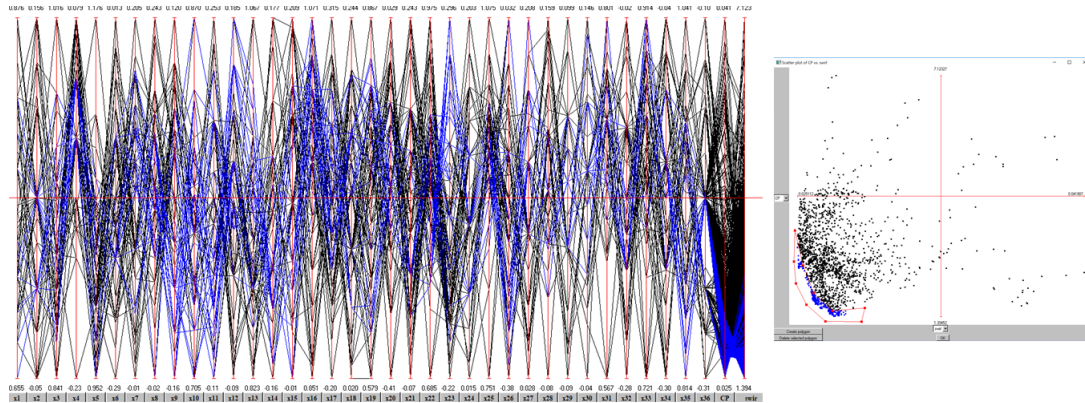


Figure 19. The complete dataset is represented in Parallel Coordinates and the two objective functions in the Scatter plot. A selection of the Pareto front is highlighted in blue.

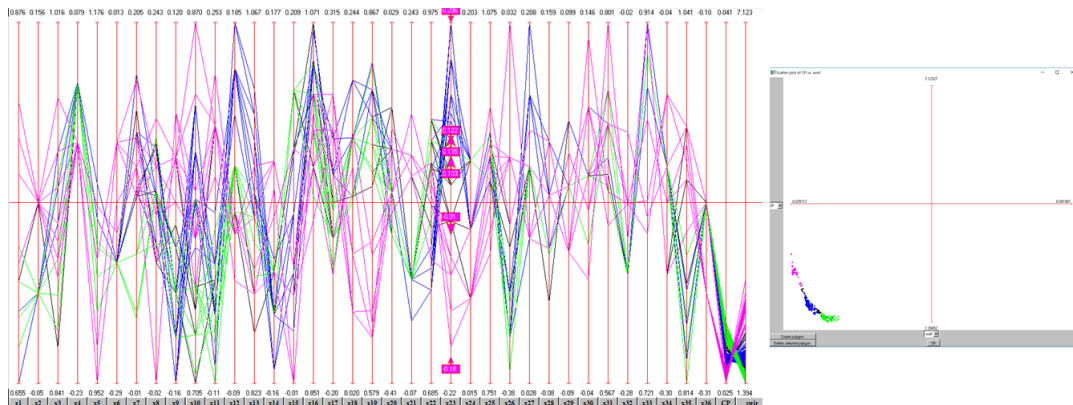


Figure 20. Three interval selections expressed for design parameter x_{23} and the reflection to the regions of optimality close to the Pareto front.

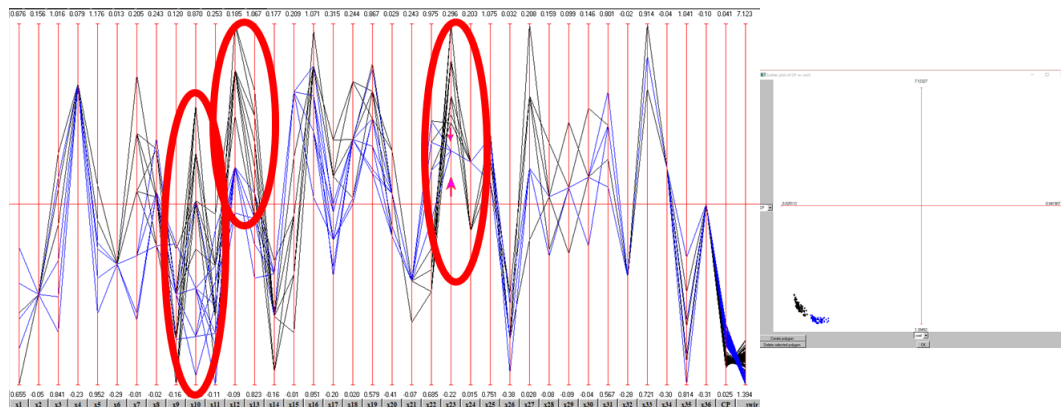


Figure 21. Comparison between the groups of solutions in the compromise region and extreme optimality for the swirl objective function (highlighted in blue).

338 If we interactively exploit in more detail the multidimensional dataset we can identify from Fig.
 339 21 that two of the three selected optimum regions exhibit very few differences, which can be analyzed
 340 in three group of parameters, x_{12} and x_{13} , x_{23} and x_{24} , and x_{10} (highlighted in red circles). These are
 341 when we select the compromise region and the one that exhibit the lowest swirl, flow distortion. In
 342 contrast, the region that exhibits the lowest pressure losses is expressed with considerable different

343 combination of the design parameters, when compared to the other two regions of the Pareto front. In
 344 Fig. 22 the differences between these sets of solutions are exposed and highlighted with red circles.

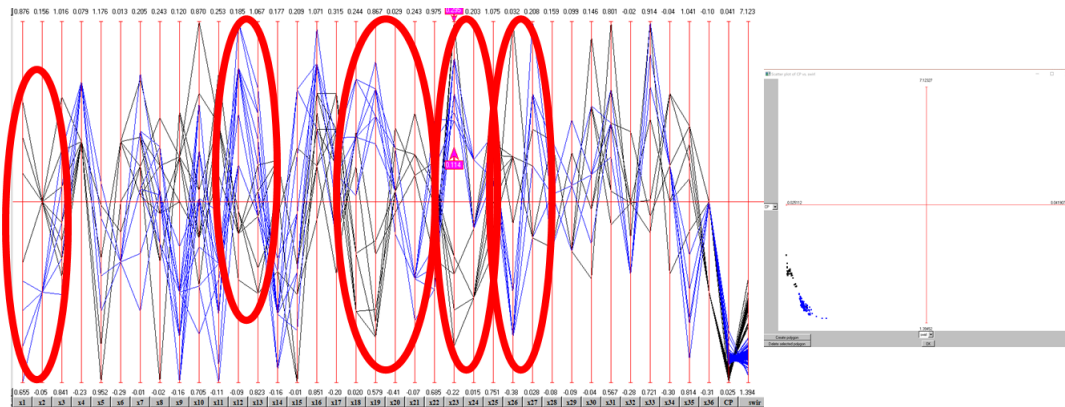


Figure 22. Comparison between the groups of solutions in the compromise region (highlighted in blue) and extreme optimality for the pressure loss objective function.

345 Hence, we can argue that two families of solutions were identified that cover the whole spectrum
 346 of optimality when we consider the flow distortion and the pressure losses.

347 5. Conclusions

348 This paper presents the computational method implemented to reduce pressure losses and flow
 349 distortion in a S-Duct. The design problem was modeled as a shape optimization study which
 350 means that the behavior of different S-Duct shapes is evaluated and compared to another considering
 351 important flow characteristics. In this case two main objective functions, that have to be minimized,
 352 were chosen: the pressure losses and the swirl. Starting from a typical S-Duct, to manage the geometry
 353 the FFD technique was employed adopting a new simple and flexible parameterization which allowed
 354 to reproduce the entire 3D duct shape with 36 decision variables. The objective functions of every
 355 deformed duct were evaluated from the result of a pressure-based steady-state RANS simulation,
 356 while the exploration of the design space was achieved using the heuristic optimization algorithm
 357 Tabu Search.

358 Results of this optimization are remarkable showing a reduction of about 14% with respect
 359 to the pressure losses and 71% with respect to the swirl angle. Compared to previous works, an
 360 extremely high improvement was achieved in terms of swirl angle, while in terms of pressure losses
 361 improvements are slightly lower. This fact is mainly due to the different parameterization approaches.
 362 The number of design variables employed in this paper are the same as in previous work, however
 363 their initial position with respect to the duct is completely different. In previous works a 3D FFD
 364 was employed embedding the duct geometry in a 3D parallelepipedic lattice. This kind of parameterization
 365 allows to exactly reproduce the original geometry, however several control points are far from the
 366 duct therefore their contribution to the duct deformation is very weak. In this paper instead the entire
 367 geometry was described using only the external duct surface, which allowed to describe a 3D geometry
 368 with a 2D formulation. In this way all the control points are almost on the duct external surface leading
 369 to a deeper and more flexible deformation.

370 Considering the optimized geometry it is possible to distinguish two main different shapes.
 371 Geometries that show best behavior in terms of pressure losses reduction, the duct cross-section shape
 372 resembles that of a rectangle. Previous works employing duct with rectangular cross-section led
 373 to extremely low values of pressure losses, therefore it is interesting to note how the optimization
 374 described in this paper lead to find a best solution in terms of CP reduction characterized by a
 375 rectangular cross-section. Instead, the extremely high reduction in terms of swirl, which was never
 376 verified in previous works, is closely linked to a triangular duct cross-section shape. Similar geometrical

377 characteristics describe the compromise optimum region as well. In this particular geometry the strong
378 area increase which occurs in the ending and lower part of the duct, due to the transition from
379 triangular to circular cross-section, exhibits the diffusing duct characteristic which leads to an overall
380 flow slowdown.

381 In this paper a total of 1300 evaluations have been performed however not all the design space has
382 been explored since the resulting Pareto front is characterized by some discontinuity. More evaluations
383 are needed to investigate more thoroughly the design space and obtain a more homogeneous Pareto
384 front. Since two main cross-section shapes have emerged from this work it could be interesting in
385 future works to study this behavior in more depth increasing the parameterization precision, i.e. the
386 numbers of design variables. This can be achieved by introducing new cross-sections or by increasing
387 the number of free control points in every cross section. Finally, further higher fidelity CFD simulations
388 could be performed in order to understand the physical behavior of such S-duct design configurations.

389 The computational design methodology is well defined and flexible enough in order to consider
390 additional or different models of objective function criteria. Hence, uncertainty quantification with
391 respect to the incoming operating conditions, but also with respect to the conditions of the exit flow
392 could be considered in future studies.

393 Abbreviations

394 The following abbreviations are used in this manuscript:

395	AIP	Aerodynamic Interface Plane
	FFD	Free-Form Deformation
396	dof	Degree of freedom
	MOTS	Multi-Objective Tabu Search

397 References

- 398 1. Liebeck R.H.. *Design of the Blended Wing Body Subsonic transport*. Journal of aircraft **2004**, Vol. 41, No. 1,.
- 399 2. Vakili A.; Jie-Zhi Wu; Liver P.; Bhat M.K.. *Measurements of compressible secondary flow in a circular S-duct*.
400 AIAA 16th Fluid and Plasma Dynamics Conference **1983**.
- 401 3. Wellborn S.R.; Reichert B. A.; Okiishi T.H.. *An experimental investigation of the flow in a diffusing S-Duct*. 28th
402 Joint Propulsion Conference and Exhibit **1992**, AIAA paper 1992-3622 .
- 403 4. Delot A.L.; Garnier E.; Pagan D.. *Flow control in a high-offset subsonic air intake*. 47th AIAA/ASME/SAE/ASEE
404 Joint Propulsion Conference & Exhibit **2011**.
- 405 5. Gissen A.N.; Vukasinovic B.; McMillan M.L.; Glezer A.. *Distortion management in a BLI inlet diffuser using*
406 *synthetic-jet hybrid flow control*. **2011**, AIAA Paper 2011-35.
- 407 6. Chierighin N.; Guglielmi L.; Savill M.; Kipouros T.; Manca E.; Rigobello A.; Barison M.; Benini E.. *Shape*
408 *Optimization of a Curved Duct with Free Form Deformations*. 23rd AIAA Computational Fluid Dynamics
409 Conference **2017**.
- 410 7. Wellborn S.R.; Okiishi T.H.; Reichert B.A.. *A study of the Compressible Flow Through a Diffusing S-Duct*. NASA
411 Technical Memorandum 106411 **1993**.
- 412 8. **Fiola C.; Agarwal K.R.. Simulation of Secondary and Separated Flow in Diffusing S Ducts. AIAA Journal of**
413 **Propulsion and Power, 2015, Vol. 31, No. 1.**
- 414 9. Delot A.L.; Scharnhorst R.K.. *A comparison of several CFD codes with experimental data in a diffusing S-Duct*.
415 49th AIAA Joint Propulsion Conference **2013**.
- 416 10. Sederberg T.W.. *Free-form deformation of solid geometric models*. 4ACM SIGGRAPH computer graphics **1986**,
417 20, 4.
- 418 11. Peachey T.C.; Kipouros T.. Monash University. *Nimrod/O user's guide* **2001-2002**.
- 419 12. Jaeggi D.M.; Parks G.T.; Kipouros T.; Clarkson P.J.. *The development of a Multi-Objective Tabu Search algorithm for*
420 *continuous optimisation problem*. European journal of operational research (EJOR) feature issue on adaptation
421 of discrete metaheuristic for continuous optimisation **2008**, Vol. 185, No. 3.

- 422 13. Tridello R.. *Comparison of genetic and tabu search algorithms in aerodynamic design of S-Duct*. Cranfield University:
423 Msc Thesis **2017**.
- 424 14. Zachos P.; MacManus D.G.; Chiereghin N.. *Flow distortion measurements in convoluted aero engine intakes*. 33rd
425 AIAA Applied Aerodynamics Conference, AIAA Aviation, Dallas, **2014**, AIAA Paper 2015-3305 .
- 426 15. Zachos P.; MacManus D.G.; Gil Prieto D.; Chiereghin N.. *Flow Distortion Measurements in Convoluted*
427 *Aeroengine Intakes*. AIAA Journal, Vols. 54, Special Section on Evaluation of RANS Solvers on Benchmark
428 Aerodynamics Flows **2014**.
- 429 16. Chiereghin N.; MacManus D.G.; Savill M.; Dupuis R.. *Dynamic distortion simulations for curved aeronautical*
430 *intakes*. Advanced Aero-concepts, Design and Operations, Royal Aeronautical Society Applied Aerodynamics
431 Conference, Bristol **2014**.
- 432 17. MacManus D.G.; Chiereghin N.; Gil Prieto D.; Zachos P.. *Complex aero-engine intake ducts and dynamic*
433 *distortion*. AIAA Aviation and Aeronautics Forum and Exposition, Dallas, USA **2014**, AIAA Paper 2015-3304.
- 434 18. Deb K.. *Multi-Objective Optimization using Evolutionary Algorithms*, Wiley **2001**.
- 435 19. Toffolo A.; Benini E.. *Genetic diversity as an objective in multi-objective evolutionary algorithms*. Massachusetts
436 Institute of Technology **2003**, Evolutionary Computation Vol. 11, No. 2.
- 437 20. Da Ronco C.C.; Benini E.. *A simplex crossover based evolutionary algorithm including the genetic diversity as*
438 *objective*. Department of Industrial Engineering, University of Padova **2001**.
- 439 21. Furlan F.; Chiereghin N.; Kipouros T.; Benini E.; Savill M.. *Computational design of S-Duct intakes for distributed*
440 *propulsion*. Aircraft engineering and aerospace technology: an international journal **2014**.
- 441 22. Inselberg A.. *Parallel Coordinates: Visual Multidimensional Geometry and Its Applications*, Springer **2009**.
- 442 23. Kipouros T.; Mleczo M.; Savill M.. *Use of Parallel Coordinates for Post-Analyses of Multi-Objective Aerodynamic*
443 *Optimisation in Turbomachinery*. AIAA Multidisciplinary Design Optimization Specialist Conference,
444 Schaumburg, USA **2008**, AIAA Paper 2008-2138.
- 445 24. Kipouros T.; Inselberg A.; Parks G. T.; Savill M.. *Parallel Coordinates in Computational Engineering Design*. AIAA
446 Multidisciplinary Design Optimization Specialist Conference, Boston, USA **2013**, AIAA Paper 2013-1750.

447 © 2018 by the authors. Submitted to MDPI for possible open access publication under the terms and conditions
448 of the Creative Commons Attribution (CC BY) license (<http://creativecommons.org/licenses/by/4.0/>).